Measurement 231 (2024) 114628

Contents lists available at ScienceDirect

Measurement

journal homepage: www.elsevier.com/locate/measurement

A procedure for the identification of effective mechanical parameters of additively manufactured elements using integrated ultrasonic bulk and guided waves

Erwin Wojtczak *, Magdalena Rucka, Angela Andrzejewska

Department of Mechanics of Materials and Structures, Faculty of Civil and Environmental Engineering, Gdańsk University of Technology, Narutowicza 11/12, 80-233 Gdańsk, Poland

ARTICLE INFO

Keywords:
Ultrasonic waves
Additive manufacturing
Dispersion curves
Effective elastic constants

ABSTRACT

The subject of the current work was a simple but robust novel two-stage procedure for the non-destructive determination of effective elastic constants using ultrasonic wave propagation. First, ultrasonic bulk wave velocities measured on cubic samples were used to calculate most of the elements of the stiffness matrix. Secondly, the remaining elements were determined using the dispersion curves of elastic guided waves measured on plate samples. Based on the complete stiffness matrix it was possible to calculate the complete set of effective elastic constants. The algorithm was verified for AM elements produced from PLA filament satisfying the conditions of transversely isotropic and orthotropic material models. For the transversely isotropic samples, Young's moduli (E) varied from 2.6 to 2.9 GPa, shear moduli (G) equalled between 0.9 and 1.2 GPa, whereas Poisson's ratios (ν) ranged between 0.20 and 0.32. In orthotropic sample the corresponding values were: E = 1.3–2.8 GPa, G = 0.6–1.2 GPa, and ν = 0.07–0.59. The results of the current study have been compared with references from the literature, giving satisfactory agreement.

1. Introduction

Additive manufacturing (AM), colloquially known as 3D printing, is becoming increasingly popular in many branches of industry. It has many bio-medical applications, e.g., in production of dental casts [1,2] or bone tissue implants [3,4]. It was also successfully used in engineering for manufacturing mechanical rotors [5,6] and so-called soft robots [7,8]. AM is a group consisting of powerful techniques that can be used to create spatial elements at different scales, from nano-particles to full-scale engineering structures. A number of different materials are used for production, such as polymers, metals, ceramics or concrete. Among many materials, biodegradable thermoplastic polymers are very popular because they do not require sophisticated equipment and are easy to manufacture. One of the common filaments is polylactic acid or polylactide (PLA). It is an eco-friendly and low cost material with a relatively low melting temperature ranging between 160 and 180 °C. Despite the simplicity of the manufacturing of 3D printed parts with PLA, there are some challenging issues that need to be addressed, e.g., the presence of local material inhomogeneities, voids or shape distortion. Damage identification and imaging, such as failure analysis of AM elements requires detailed analyses, e.g., using numerical simulations, which require an appropriate description of the structure and the elastic behaviour of the AM elements.

In order to mechanically characterise 3D printed samples, which are generally heterogeneous, it is necessary to accurately model their micro- and macrostructure, including filament orientation, the presence of voids, and, if appropriate, inserts, such as carbon or wood fibres. However, for many applications, it is sufficient to use a simplified approach, i.e., material homogenization, which allows the exact heterogeneous model to be replaced with the homogeneous one described by effective elastic parameters. A number of works can be reported that use this approach to characterise the static behaviour of 3D printed elements. Biswas et al. [9] analysed the mechanical response of ABS samples printed with different raster angles. They performed finite element simulations using micromechanical models prepared based on micro-CT scans to determine the elastic constants of the samples using the homogenized orthotropic material model. Gonabadi et al. [10] predicted the macro-scale elastic response of 3D printed samples made of PLA based on finite elements modelling of the real sample microstructure. The models were prepared to determine the elastic constants

* Corresponding author.
E-mail addresses: erwin.wojtczak@pg.edu.pl (E. Wojtczak), magdalena.rucka@pg.edu.pl (M. Rucka), angela.andrzejewska@pg.edu.pl (A. Andrzejewska).

https://doi.org/10.1016/j.measurement.2024.114628
Received 24 November 2023; Received in revised form 15 March 2024; Accepted 29 March 2024
Available online 29 March 2024

of an orthotropic material model based on a tensile test, 3-point bending and Iosipescu shear tests. Lei et al. [11] analysed the influence of printing parameters on the mechanical behaviour of samples made of PLA reinforced with carbon fibres. They used scanning electron microscope images to reveal the internal structure of the samples and carried out material homogenization, assuming an orthotropic material model. Torre et al. [12] considered the behaviour of PLA samples under tensile, simple bending, three-point bending and bending-torsion tests. They determined the elastic parameters of the samples by treating them as orthotropic. Sabik et al. [13] determined the effective elastic constants of PLA samples based on static tensile tests using a transversely isotropic model. They considered the tensile failure of the dogbone samples using experimental and theoretical approaches.

The above-reported works show the results of numerical simulations and destructive testing. However, a current trend is to use non-destructive testing (NDT) measurements, which are very promising because they can be repeated many times without damaging the samples. One of the NDT techniques with a number of efficient applications for investigation of 3D printed elements is a vibrational method, based on the low-frequency vibration response. Piovan et al. [14] considered the identification of the effective bending elastic modulus of parallelepiped samples produced from PLA filament. They also characterised the dynamic behaviour of U-shaped beams experimentally and with finite element models. Medel et al. [15] determined the equivalent elastic modulus of PLA samples. They discussed the influence of different printing parameters (raster angle, build orientation, layer height, printing speed and nozzle temperature) on the dynamic behaviour of rectangular prisms. Krivic and Slavič [16] proposed the simultaneous identification of elastic modulus, damping and coefficient of thermal expansion of samples produced from different filaments, including PLA, PETG and nylon. They integrated different measurement techniques such as digital image correlation, scanning laser Doppler vibrometry (SLDV) and vibration testing to investigate samples with a specific geometry. The works described above mostly deal with the problem of determining a single value of the elastic modulus, i.e., equivalent bending elastic modulus, which is not sufficient for the complete characterisation of the material. A complete set of orthotropic elastic constants was determined using the vibrational technique by Huang and Lin [17]. They determined the elastic constants of PLA from the natural frequencies of the bending and torsional vibration modes, using the simplification that the Young's modulus, shear modulus and Poisson's ratio in each plane of symmetry satisfy the relation applicable to isotropic materials.

The elastic parameters of different materials can be effectively obtained by another promising NDT technique, using the propagation of bulk and guided ultrasonic waves. Bulk waves have been used by many authors to determine the isotropic elastic constants of concrete elements [18–20] or adhesives [21–23]. Guided wave measurements have been successfully used to characterise the elastic behaviour of different elements, among many, adhesive joints [24–26] or composites [27–29]. In particular, Lamb wave dispersion curves have been used to determine the elastic constants of various elements described by the isotropic [30–32], transversely isotropic [33–35], and orthotropic [36–38] material models. Some applications of ultrasonic waves for the material characterisation of AM elements can also be reported. Foster et al. [39] evaluated the elastic constants of aluminium samples produced by ultrasonic additive manufacturing. They determined the effective stiffness constants using ultrasonic wave velocities. Javidrad and Salemi [40] used longitudinal and transverse waves to determine the elastic constants of Inconel 625 samples produced using a laser powder-bed fusion process. They verified the results with static tensile tests.

The current state-of-the-art shows that the number of works considering NDT techniques for the determination of elastic constants of 3D printed samples is limited. A lack of straightforward and effective approach for characterization of elastic response of AM elements is observed. The original contribution of the current work is the simple but robust novel ultrasonic wave-based procedure for non-destructive identification of effective elastic constants of additively manufactured samples treated as homogenized material. Based on the fabrication process of the samples, transversely isotropic and orthotropic material models were used to describe the mechanical behaviour of the samples. The set of carefully designed experiments performed on PLA samples produced with different raster angles was reported. Two fundamental phenomena using elastic waves were considered, i.e., bulk wave propagation in volumetric samples and guided wave propagation in plates. Additionally, theoretical calculations of guided wave dispersion curves were carried out using the semi-analytical finite element (SAFE) method. The results proved that ultrasonic waves can be used for fast and effective characterisation of AM elements. The results of the performed study are intended for further use in damage imaging and failure analysis of these types of elements.

2. Ultrasonic wave-based identification of elastic parameters

The phenomenon of elastic wave propagation is strongly dependent on the mechanical properties of the medium in which it occurs. Thanks to this fact, it is possible to determine the constitutive matrix **C** of the medium based on the wave characteristics. It is well known that in unbounded media so-called bulk waves propagate, i.e., P-waves (pressure or longitudinal waves) and S-waves (shear or transverse waves). Both waves propagate with different velocities, commonly denoted as c_L and c_T, respectively. One of the methods utilizing bulk waves is ultrasonic pulse velocity (UPV) which allows one to determine the time of flight (TOF) of the wave through a volumetric sample (e.g., cube or cylinder). Based on the TOF and the length of the propagation path d (distance between the transmitting and receiving transducers) it is possible to determine the wave velocity as:

$$c_i = \frac{d}{TOF}, \quad i = L, T. \tag{1}$$

The bulk wave velocities can be used to define some elements of stiffness matrix **C**, but are generally not sufficient to determine the full matrix when considering more complex material models than isotropic. The quasi-longitudinal and quasi-transverse waves can be used to overcome this problem, however, specifically shaped samples are required [40].

In restrained media, such as plates, shells or rods, so-called guided waves occur. These waves are characterised by multimodality and dispersion (frequency-dependence), i.e., at a given frequency a number of wave modes can propagate simultaneously with different velocities. The relation between wave characteristics and frequency can be represented graphically as dispersion curves. The guided wave dispersion curves can be determined experimentally, and, by comparison with theoretical results, allow the characterisation of the elastic constants. The shape of dispersion curves can be used to derive the constitutive matrix **C**, but depending on the complexity of the material model, carrying it out using only dispersion curves can be a difficult multidimensional optimization problem. For a homogeneous isotropic material, only two material constants need to be described. However, in the case of 3D printed elements, which are usually not characterised by isotropy, more complex approaches are required, including transverse isotropy or orthotropy.

Taking into account the factors described above, it is proposed to use both bulk waves and guided waves to determine the constitutive matrix **C** and then the elastic constants. A novel algorithm (Fig. 1) is introduced to simplify the analysis. The procedure requires the production of two types of samples – cube and plate, prepared with the same printing parameters. First, the cubic sample is investigated using the UPV analyzer to determine the TOF of the wave. Knowing the sample geometry, it is possible to calculate the wave velocity using formula (1). The obtained velocities of pressure and shear waves, together with the mass density of the sample, allow some elements of the **C** matrix to be

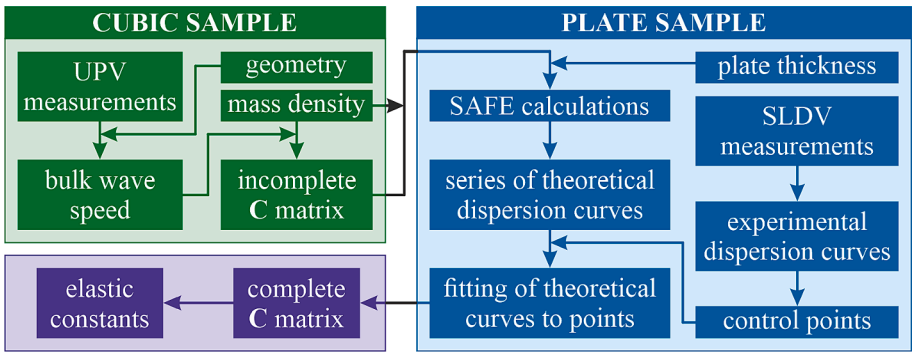

Fig. 1. Scheme of the proposed algorithm for ultrasonic wave-based identification of mechanical parameters of 3D printed samples.

calculated, however, in general, it is not possible to obtain the complete matrix only from measurements of a single volumetric sample. Depending on the complexity of the material model, some of the elements remain unknown.

Independently, the plate sample is investigated to determine the experimental dispersion curves. A powerful and commonly used method is to measure the series of signals on the surface of the sample using scanning laser Doppler vibrometry, supported by further signal processing using two-dimensional fast Fourier transform (2D-FFT) [41–45]. The result of the calculations are dispersion curves in the form of a 2D map in the frequency-wavenumber domain. For further processing, curve tracing algorithms are required. However, in the current study, it is proposed to extract only a small number of n points from each curve, taken at specific frequencies. This approach can be useful, especially in cases where experimental dispersion curves may not be visualized with the same quality over the entire assumed frequency range. The previously determined **C** matrix based on bulk waves (with some unknown elements), together with mass density and plate thickness can be used for the calculation of theoretical dispersion curves. There are a number of techniques capable of calculating theoretical dispersion curves, including the SAFE method [46,47]. Several calculations are required with different values of the unknown parameters of the **C** matrix. The series of theoretical dispersion curves obtained are then compared with the experimental curves (represented by previously determined control points) to obtain the best fit. Considering the fact, that the SAFE calculations provide the dispersion curves in the form of a disordered set of points not related to individual curves, for each i-th control point at a given frequency, a theoretical wavenumber value $k_{t,i}$ closest to the experimental $k_{e,i}$ is found (without considering whether the curve is appropriate – if it is not a good curve, the error will increase anyway). Then the sum of squared errors is calculated for all n control points according to the formula [31]:

$$RSS = \sum_{i=1}^{n} \left(k_{e,i} - k_{t,i}\right)^2. \tag{2}$$

The minimization of the RSS function allows the missing elements and the complete **C** matrix to be determined. Depending on the assumed material model, a certain number of elastic constants can be further calculated.

2.1. Ultrasonic waves in an orthotropic medium

In the case of an orthotropic material, three orthogonal planes of symmetry can be distinguished. The mechanical properties are unique and differ along three perpendicular directions 1, 2, 3 (Fig. 2).

The stiffness matrix **C** characterizing the orthotropic material contains nine independent elastic constants: C_{11}, C_{22}, C_{33}, C_{12}, C_{13}, C_{23}, C_{44}, C_{55}, C_{66}, represented in **C** as [48]:

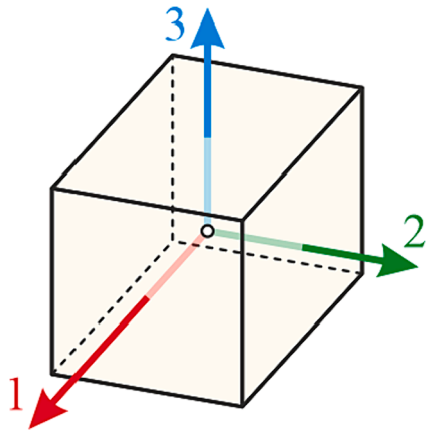

Fig. 2. Designation of material axes in orthotropic material.

$$\mathbf{C} = \begin{bmatrix} C_{11} & C_{12} & C_{13} & 0 & 0 & 0 \\ C_{12} & C_{22} & C_{23} & 0 & 0 & 0 \\ C_{13} & C_{23} & C_{33} & 0 & 0 & 0 \\ 0 & 0 & 0 & C_{44} & 0 & 0 \\ 0 & 0 & 0 & 0 & C_{55} & 0 \\ 0 & 0 & 0 & 0 & 0 & C_{66} \end{bmatrix}. \tag{3}$$

The stiffness matrix **C** is essential for the determination of theoretical dispersion curves of guided waves and can be used to determine theoretical values of wave velocities of bulk waves. The velocities of bulk waves along three axes in orthotropic material are given in Table 1.

It is evident that only six of the nine parameters are present in the equations, so measuring the wave velocities along three axes is not sufficient to determine the full matrix **C**. For this reason, guided wave dispersion curves are required, because guided wave propagation depends on the complete matrix. Therefore, three additional parameters need to be determined.

In order to determine the elastic constants, it is useful to invert the stiffness matrix **C** to obtain the compliance matrix **S** [48]:

Table 1
P-wave and S-wave velocities in the orthotropic medium [48].

Direction (axis)	P-wave velocity	S-wave velocity	
Along 1	$c_{L,1} = \sqrt{\frac{C_{11}}{\rho}}$	$c_{T,12} = \sqrt{\frac{C_{66}}{\rho}}$	$c_{T,13} = \sqrt{\frac{C_{55}}{\rho}}$
Along 2	$c_{L,2} = \sqrt{\frac{C_{22}}{\rho}}$	$c_{T,21} = \sqrt{\frac{C_{66}}{\rho}}$	$c_{T,23} = \sqrt{\frac{C_{44}}{\rho}}$
Along 3	$c_{L,3} = \sqrt{\frac{C_{33}}{\rho}}$	$c_{T,31} = \sqrt{\frac{C_{55}}{\rho}}$	$c_{T,32} = \sqrt{\frac{C_{44}}{\rho}}$

$$\mathbf{S} = \begin{bmatrix} 1/E_1 & -\nu_{12}/E_1 & -\nu_{13}/E_1 & 0 & 0 & 0 \\ -\nu_{21}/E_2 & 1/E_2 & -\nu_{23}/E_2 & 0 & 0 & 0 \\ -\nu_{31}/E_3 & -\nu_{32}/E_3 & 1/E_3 & 0 & 0 & 0 \\ 0 & 0 & 0 & 1/G_{23} & 0 & 0 \\ 0 & 0 & 0 & 0 & 1/G_{31} & 0 \\ 0 & 0 & 0 & 0 & 0 & 1/G_{12} \end{bmatrix}, \tag{4}$$

from which it is possible to determine the elastic constants, i.e., three Young's moduli E_1, E_2, E_3, three shear moduli G_{23}, G_{31}, G_{12} and six Poisson's ratios ν_{12}, ν_{21}, ν_{13}, ν_{31}, ν_{23}, ν_{32}, which are pairwise dependent (in fact, nine independent constants are needed to characterize the material).

2.2. Ultrasonic waves in a transversely isotropic medium

Transverse isotropy is a specific example of orthotropy where two of the directions are equivalent, thus one axis of symmetry and two transverse axes are distinguished, forming a plane of isotropy. Suppose that the symmetry axis is 3 and the other two (1, 2) are transverse axes (see Fig. 2). Compared to the orthotropic model, the problem is simplified from nine independent constants to five, i.e., C_{11}, C_{33}, C_{12}, C_{13}, C_{44}. The stiffness matrix has the form [48]:

$$\mathbf{C} = \begin{bmatrix} C_{11} & C_{12} & C_{13} & 0 & 0 & 0 \\ C_{12} & C_{11} & C_{13} & 0 & 0 & 0 \\ C_{13} & C_{13} & C_{33} & 0 & 0 & 0 \\ 0 & 0 & 0 & C_{44} & 0 & 0 \\ 0 & 0 & 0 & 0 & C_{44} & 0 \\ 0 & 0 & 0 & 0 & 0 & \dfrac{C_{11}-C_{12}}{2} \end{bmatrix}. \tag{5}$$

The bulk wave velocities along the axes of the transversely isotropic medium are given in Table 2. There are two P-waves travelling with different velocities (one along the symmetry axis and two along the transverse axes with equal velocities). One S-wave travels along the symmetry axis and two different S-waves propagate along the transverse axes, depending on the direction of particle motion (one in the plane of isotropy and one out of this plane). Four different wave velocities allow determining four of the five elements of **C**. Only C_{13} is missing, which can be determined based on the dispersion curves.

Knowing the exact form of the **C** matrix, the elastic constants can be calculated using the compliance matrix **S** (inverse of **C**), as proposed for the orthotropic model, however, they can also be determined directly from the stiffness matrix [49]. Young's moduli (along transverse axes E_1 and symmetry axis E_3) are calculated according to the formulae:

$$E_1 = \frac{(C_{11}-C_{12})\left((C_{11}+C_{12})C_{33}-2C_{13}^2\right)}{C_{11}C_{33}-C_{13}^2}, \qquad E_3 = C_{33} - \frac{2C_{13}^2}{C_{11}+C_{12}}. \tag{6}$$

Shear moduli out of the plane of isotropy G_{31} and in this plane G_{12} are:

$$G_{31} = C_{44}, \qquad G_{12} = \frac{C_{11}-C_{12}}{2}. \tag{7}$$

Table 2
P-wave and S-wave velocities in the transversely isotropic medium [48].

Direction (axis)	P-wave velocity	S-wave velocity	
Along 1	$c_{L,1} = \sqrt{\frac{C_{11}}{\rho}}$	$c_{T,12} = \sqrt{\frac{C_{11}-C_{12}}{2\rho}}$	$c_{T,13} = \sqrt{\frac{C_{44}}{\rho}}$
Along 2	$c_{L,2} = \sqrt{\frac{C_{11}}{\rho}}$	$c_{T,21} = \sqrt{\frac{C_{11}-C_{12}}{2\rho}}$	$c_{T,23} = \sqrt{\frac{C_{44}}{\rho}}$
Along 3	$c_{L,3} = \sqrt{\frac{C_{33}}{\rho}}$	$c_{T,31} = c_{T,32} = \sqrt{\frac{C_{44}}{\rho}}$	

Poisson's ratio out of the plane of isotropy ν_{31} is:

$$\nu_{31} = \frac{C_{13}}{C_{11}+C_{12}}. \tag{8}$$

Additionally, two dependent Poisson's ratios, the second out of the plane of isotropy ν_{13} and in the plane of isotropy ν_{12} can be calculated as:

$$\nu_{13} = \frac{E_1}{E_3}\nu_{31}, \qquad \nu_{12} = \frac{E_1}{2G_{12}} - 1. \tag{9}$$

3. Experimental investigations

3.1. Object of research

The research was conducted on additively manufactured samples produced using fused filament fabrication (FFF) method from polylactic acid with the use of UltiMaker 3 Extended (Utrecht, The Netherlands). The PLA filament with a diameter of 2.85 mm was manufactured by UltiMaker. Three variants of infill pattern were considered (#1–3, as shown in Fig. 3a), differing in the direction of filament deposition (see Table 3). The raster angles with respect to the sample x-axis in two consecutive layers were: 0°/90° (#1), 45°/-45° (#2) and 90°/90° (#3). First two variants were selected as typical due to the symmetry of the directions in printing plane. The third one was chosen to verify the possibilities and limitations of the currently developed method. The layers were produced one by one along the z-axis with 100 % infill with the printing speed of 3600 mm/min. The nozzle diameter was 0.4 mm. To ensure the print quality of the specimens, a layer thickness of 0.1 mm and the line width of 0.4 mm were used. The temperatures used for the 3D printing process were around 60 °C for the building platform and 220 °C for the printing nozzle. The samples were manufactured without top and bottom solid layers, and also without the perimeter outlines to avoid their influence on the results, thus the analysis refers only to the layers produced as infill. In order to determine the mechanical parameters, two types of samples were produced for each manufacturing variant. The first was the cubic samples, denoted as #C1-3 (Fig. 3b), with designed dimensions of 50 × 50 × 50 mm^3. Exact dimensions, such as mass and mass density of the samples are given in Table 3. In addition, plate samples were produced (Fig. 3c) with an area of 100 × 180 mm^2 and a designed thickness of 3 mm. The measured thicknesses for the plates produced were: t = 3.07 mm (#P1), t = 3.09 mm (#P2) and t = 3.11 mm (#P3).

3.2. Experimental setup and procedure

3.2.1. Ultrasonic pulse velocity analyzer

The measurements of ultrasonic bulk wave velocities were conducted using the ultrasonic pulse velocity tester Pundit PL-200 (Proceq). The device, shown in Fig. 4a, uses the through-transmission technique, i.

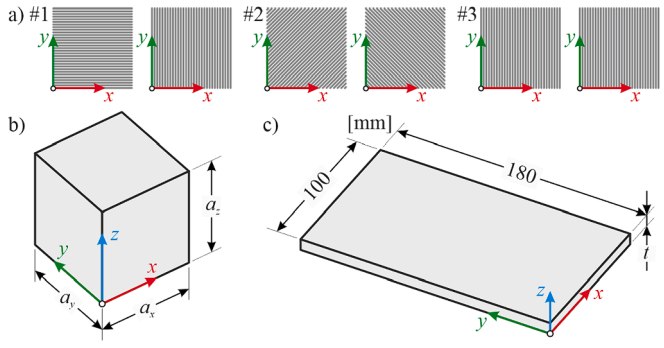

Fig. 3. Object of research: a) sample infill in two consecutive layers (variants #1–3), b) geometry of cubic samples, c) geometry of plate samples.

Table 3
Parameters of samples used for experimental investigations.

Printing Variant	Raster angles	Cubic Samples						Plate samples	
		Symbol	a_x [mm]	a_y [mm]	a_z [mm]	m [g]	ρ [kg/m^3]	Symbol	t [mm]
#1	0°/90°	**#C1**	49.5	49.6	50.0	130.4	1062	**#P1**	3.07
#2	45°/-45°	**#C2**	49.5	49.5	50.1	133.7	1089	**#P2**	3.09
#3	90°/90°	**#C3**	48.5	49.5	50.1	132.1	1098	**#P3**	3.11

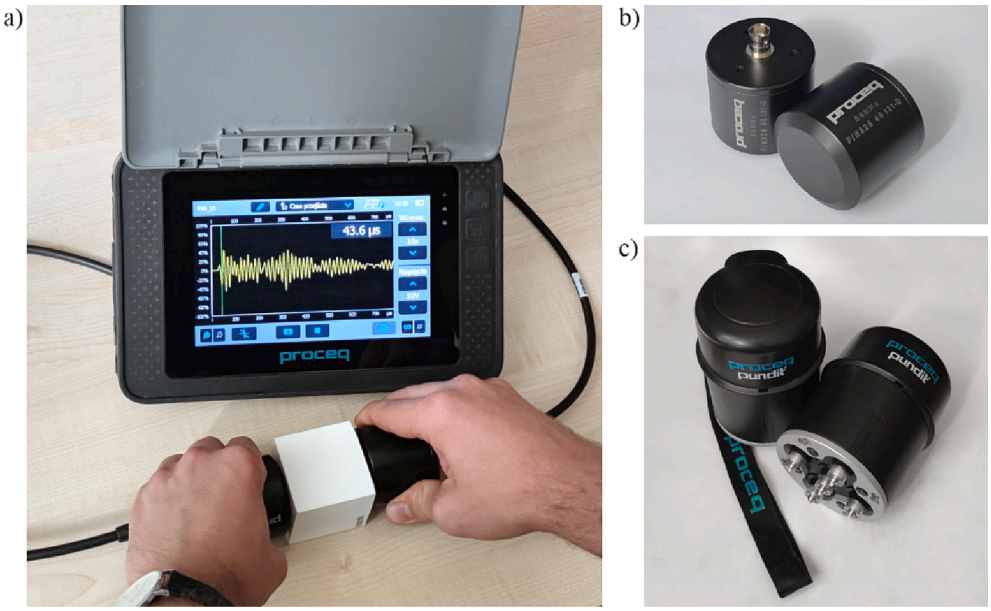

Fig. 4. Experimental setup for the determination of bulk wave velocities: a) measurement with Pundit PL-200 UPV tester on a cubic sample, b) P-wave transducers (54 kHz), c) S-wave transducers (40 kHz).

e., a pair of transducers is required to evaluate the TOF of the wave. To determine the TOF of the P-wave, standard single-crystal probes with a diameter of 49.7 mm emitting a wave with a central frequency of 54 kHz (Fig. 4b) were used. A gel couplant was used to ensure the appropriate contact between transducer and sample surface for effective propagation of the wave through the sample. In the case of S-wave measurements, dry-point contact probes with 5 dual-crystal transducers with a central frequency of 40 kHz were chosen (Fig. 4c), where the distance between the two furthest transducers was 47 mm. The dimensions of the contact face of both types of probes were smaller than each face of the cubic sample. The dimensions of the samples tested met the requirement of at least exceeding the wavelength, which was expected to be equal to 37 mm for the P-wave (assuming $c_{L,\max} = 2000$ m/s) and 30 mm for the S-wave (assuming $c_{T,\max} = 1200$ m/s).

The TOF of the P-wave was measured along each of the three axes (x, y, z) by placing the 54 kHz probes on each pair of faces of the tested cubes (y-z, x-z, x-y, respectively). Three independent measurements were made on each face to eliminate random measurement errors. Since it is known that the direction of wave propagation and the direction of particle motion of shear wave are perpendicular, the measurements with 40 kHz probes were carried out at each sample face i-j (along axis k) for two orientations of probes, generating two shear waves independently, i. e., in the i-k plane and in the j-k plane ($i, j, k = [x, y, z], i \neq j, i \neq k, j \neq k$). The TOF of each S-wave was determined four times. The complete set of experimental data obtained from UPV measurements is available at [50].

3.2.2. *Scanning laser Doppler vibrometry*

The measurements of ultrasonic guided wave propagation were conducted using the SLDV technique. The experimental set-up is presented in Fig. 5a. The input signals were provided by the arbitrary function generator AFG 3022 (Tektronix, Inc.) and amplified by the high-voltage amplifier PPA 2000 (EC Electronics). Each excitation signal was in the form of a wave packet produced by the windowing of a single-cycle sine function with a raised cosine (Hann) window. Different carrier frequencies were used, namely, 50 kHz, 100 kHz, 150 kHz, 200 kHz, and 250 kHz. The waves were excited with the use of NAC2024 (Noliac) piezoelectric actuators with dimensions of $3 \times 3 \times 2$ mm^2, made of lead zirconate titanate (PZT) compound. The actuators were attached to each plate sample with petro wax 080A109 (PCB Piezotronics, Inc.) to ensure correct coupling. Two measurement scenarios were assumed to independently excite different types of dominant waves, using different locations of the PZT actuators. First, the elastic waves were excited in the plane of the sample, inducing mainly symmetric modes using the S-type actuator. Secondly, the waves were excited perpendicular to the plate surface, to better capture the antisymmetric modes (A-type actuator). The signals of the propagating waves (out-of-plane velocity component) were remotely collected at the upper surface of each plate by the scanning head of the laser vibrometer PSV-3D-400-M (Polytec GmbH) equipped with a VD-07 velocity decoder. The signals were recorded at 91 points distributed along a straight line with a length of 90 mm. The scanned area of each sample was covered with *retro*-reflective sheeting to improve the light backscatter. The sampling frequency of the recorded signals was 2.56 MHz. The signals were measured and averaged 20 times to reduce the influence of signal noise. The time interval between two consecutive measurements at each point equalled 100 ms to ensure appropriate attenuation of wave signal, giving a total measurement time of 2 s for each measurement point. Each plate (#P1-3) was tested according to the scheme presented in Fig. 5b (actuators on the shorter side of a plate, measurements along the y axis, using trace line A).

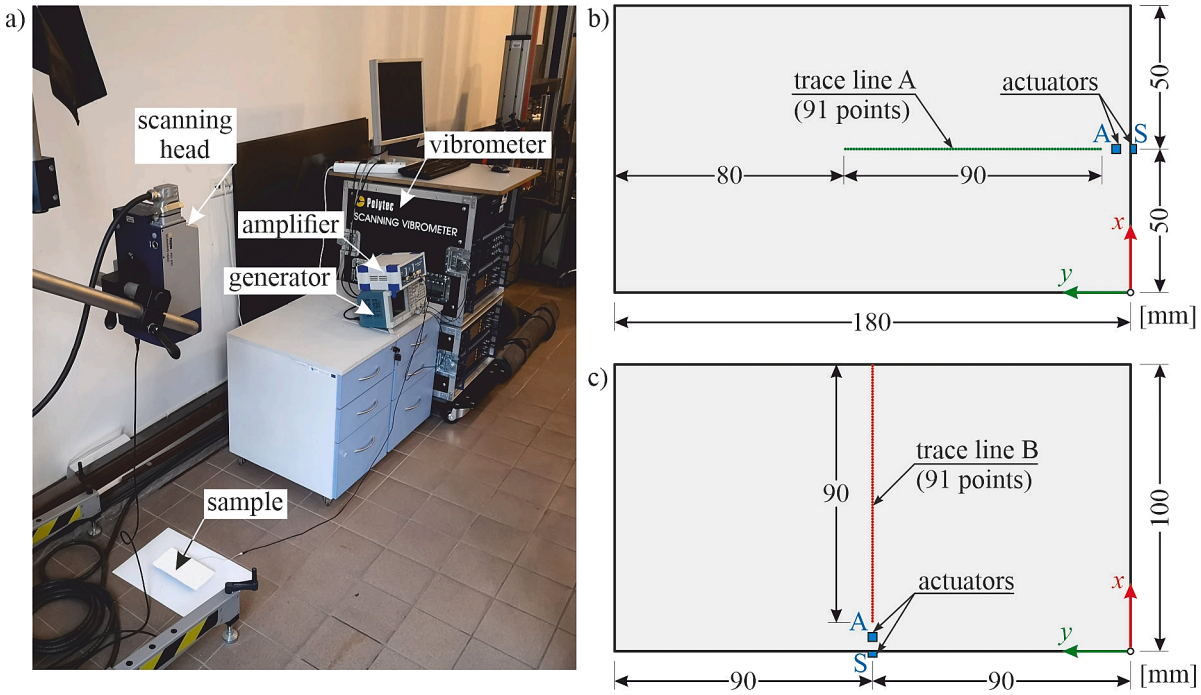

Fig. 5. Experimental set-up for the determination of dispersion curves in plate samples (a); scheme of scanning points with trace A (b) and trace B (c).

Additionally, plate #P3 was tested using the scheme presented in Fig. 5c (actuators on the longer side of a plate, measurement along the x axis, using trace line B) due to the fact that the x and y axes were not equivalent in this sample (unlike for samples #P1 and #P2). The complete set of experimental data gathered by the laser vibrometer in the course of the guided wave measurements is available at [50].

As a result of each experimental measurement, a guided wavefield $w_0(x,t)$ in the space (x) and time (t) domain was acquired. In order to obtain dispersion curves, the first step was to expand the dataset in the space domain by adding zero vectors (so-called zero-padding). The two-dimensional fast Fourier transform (2D-FFT) was then applied to the expanded dataset $w(x,t)$ allowing the wavenumber-frequency (k-f) relation to be obtained, according to the formula [41–45]:

$$D(k,f) = \iint w(x,t)\mathrm{e}^{-i2\pi(kx+ft)}\mathrm{d}x\mathrm{d}t, \tag{10}$$

where $D(k,f)$ are the Fourier coefficients. The map representing the relation of D vs. k and f enabled the identification of the specific wave modes. For a number of independent measurements, allowing to plot dispersion curves in different frequency ranges, the 2D-FFT calculations were performed independently and then, all maps were aggregated to obtain complete dispersion curves.

4. Results and discussion

4.1. UPV measurements

The P-wave and S-wave velocities were determined from Eq. (1) based on the TOFs of the bulk waves obtained from the UPV tests and the exact dimensions of cubic samples #C1-3 (see Table 3). As there was more than one measurement for each type of wave, the final velocity values were averaged. The results for all samples are presented in Table 4. Three P-wave velocities (one along each of the x,y and z axes) and six S-wave velocities (two along each axis, with perpendicular directions of particle motion) were determined for all cubes. In the shear wave symbols, the indices denote the directions of wave propagation and particle motion, respectively. The S-wave velocities along the x-axis for sample #C3 were not calculated, because the corresponding signals were of low quality due to the infill pattern, making it impossible to determine the TOF. It is important to note that the resulting wave velocities did not exceed the limit used to calculate the minimum specimen size in Section 3.2.1, thus the measurements were conducted properly.

4.2. Transversely isotropic material model (variants #1 and #2)

4.2.1. Identification of mechanical parameters based on bulk wave velocities

Taking into account the fabrication process of the samples in variants #1 and #2, they met the requirements of a transversely isotropic material model. The mechanical properties in the x-y plane should be equal, so it was assumed to be the plane of isotropy, whereas the third axis (z) was an axis of symmetry. This assumption was confirmed by the fact that the P-wave velocities in the x and y directions were almost identical (the difference between $c_{L,x}$ and $c_{L,y}$ with respect to their mean value was equal to 0.20 % for #1 and 0.12 % for #2), so the mean value, denoted as $c_{L,1}$, was assumed for further considerations. Moreover, S-wave velocities in the x-y plane ($c_{T,x(y)}$ and $c_{T,y(x)}$) were similar (relative difference equal to 0.10 % for #1 and 0.06 % for #2), so they were averaged and

Table 4
P-wave and S-wave velocities for cubic samples #C1-3.

Sample	$c_{L,x}$ [m/s]	$c_{L,y}$ [m/s]	$c_{L,z}$ [m/s]	$c_{T,x(y)}$ [m/s]	$c_{T,x(z)}$ [m/s]	$c_{T,y(x)}$ [m/s]	$c_{T,y(z)}$ [m/s]	$c_{T,z(x)}$ [m/s]	$c_{T,z(y)}$ [m/s]
#C1	1828.8	1832.5	1766.8	1043.8	919.6	1044.8	923.2	917.4	922.5
#C2	1767.9	1770.0	1862.5	1028.6	949.6	1028.0	950.6	952.0	948.4
#C3	1368.1	1815.4	1733.6	—*	—*	880.0	1037.2	720.9	1047.6

* signals corresponding with these velocities were not legible, and TOFs were impossible to be determined reliably.

Table 5
P-wave and S-wave velocities for samples printed in variants #1–2 (transversely isotropic material model).

Variant	$c_{L,1}$ [m/s]	$c_{L,3}$ [m/s]	$c_{T,12}$ [m/s]	$c_{T,13}$ [m/s]
#1	1830.7	1766.8	1044.3	920.7
#2	1768.9	1862.5	1028.3	950.2

denoted as $c_{T,12}$. It was also expected that the S-wave velocities in the two remaining planes (x-z, y-z) should be equal in pairs and indeed they were (the relative difference between the extreme values with respect to the mean value was 0.63 % for #1 and 0.38 % for #2), so they were averaged and denoted as $c_{T,13}$. As a result, four independent values of wave velocities were used for the characterisation of the elastic behaviour of samples printed with #1 and #2 variants (Table 5).

Since there were four different velocities, only four of the five independent coefficients of stiffness matrix **C** could be calculated. According to the formulae in Table 2, the following elements were equal: $C_{11} = 3.559$ GPa, $C_{33} = 3.315$ GPa, $C_{12} = 1.243$ GPa, $C_{44} = 0.900$ GPa (for #1) and $C_{11} = 3.407$ GPa, $C_{33} = 3.778$ GPa, $C_{12} = 1.104$ GPa, $C_{44} = 0.983$ GPa (for #2). The only undefined element was C_{13} because it was not present in the equations in Table 2.

4.2.2. *Identification of remaining mechanical parameters based on dispersion curves*

The guided wave dispersion curves measured for plate samples #P1 and #P2 were used to determine the missing element C_{13} of the stiffness matrix. First, 2D-FFT calculations were performed and, as a result, a two-dimensional representation of the wavenumber versus frequency relation was visualised for both plates (Fig. 6). It can be clearly seen that the quality of the maps allows the identification of curves associated with specific wave modes. For each curve, control points were determined for characteristic frequencies equal to: 50 kHz, 150 kHz, 250 kHz, and 350 kHz (see Fig. 6).

Independently, a series of calculations of theoretical dispersion curves were performed using an authorial script written in Matlab®, utilizing the SAFE method. The stiffness matrix containing elements C_{11}, C_{33}, C_{12}, and C_{44} determined in the previous section was used. The missing coefficient C_{13} was assumed to be in the range between 0 GPa and 2 GPa with a step of 0.001 GPa. For each control point read from the experimental dispersion curves (with value $k_{e,i}$), the nearest point of the theoretical curves (with value $k_{t,i}$) was found. The RSS function, representing the squared differences between experimental and theoretical values, was then calculated based on Eq. (2). The RSS was used as an objective function and was minimised as it represents the divergence between experimental and theoretical results. The relation between RSS and C_{13} for both variants #1 and #2 is presented in Fig. 7. Clear minima are visible in both diagrams. The optimum values of C_{13} were determined, which were 1.334 GPa for variant #1 and 1.437 GPa for variant #2. It can be seen that the functions are locally sharp which may be due to the fact that multiple curves appear in the SAFE results and some points may falsely indicate a slightly lower RSS while the wrong curve is fitted. However, this effect is rather small for the global result.

Since the SAFE method, in its simplest approach, does not provide an adequate separation of specific curves and all waves modes are coupled, including, for example, curves for horizontal or vertical shear waves (not considered in the current research), an authorial algorithm was prepared in Matlab® to extract only curves corresponding to the symmetric and antisymmetric wave modes. First, the visual identification of each curve of interest was performed. Second, a two starting points, i.e., points of the curve corresponding to its origin, were determined and the difference quotient was calculated for them. Then, using the fact that dispersion curves are smooth, the following points were determined as points with the closest different quotient to the original two. This step

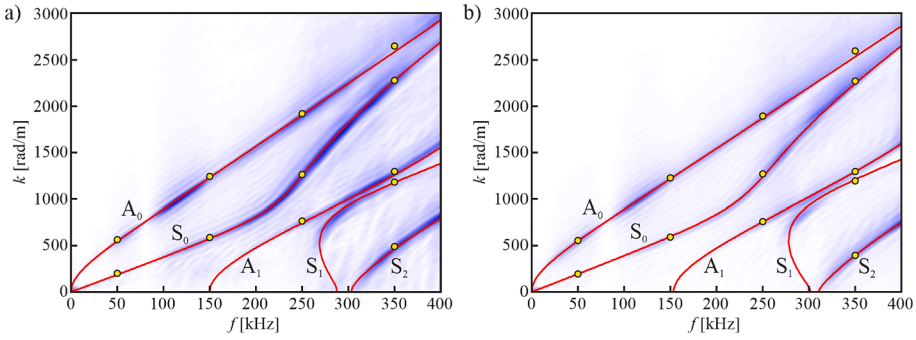

Fig. 6. Experimental dispersion curves (2D-FFT white-blue map) with control points (yellow circles) and theoretical dispersion curves from SAFE (red lines): a) plate #P1, b) plate #P2.

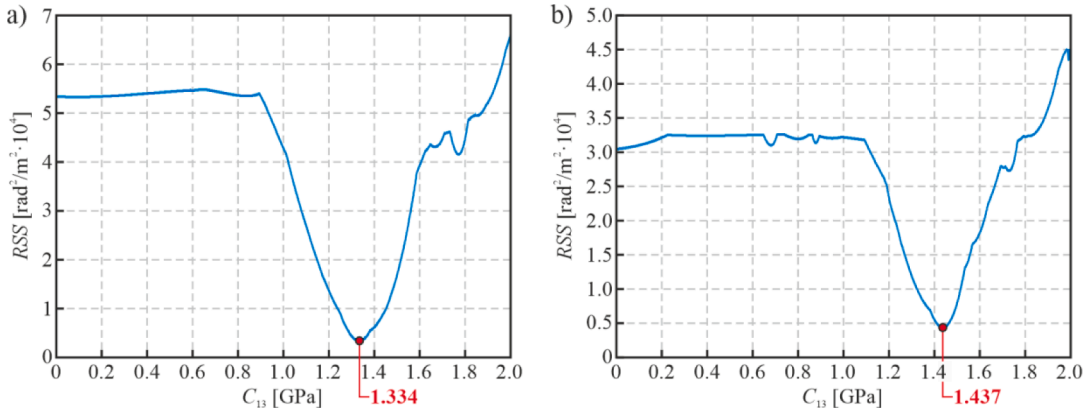

Fig. 7. Relation between RSS and C_{13} element of stiffness matrix **C**: a) variant #1 (sample #P1), b) variant #2 (sample #P2).

Table 6
Elements of constitutive matrix **C** of samples printed in variants #1 and #2 (transversely isotropic material model).

Variant	C_{11} [GPa]	C_{33} [GPa]	C_{12} [GPa]	C_{13} [GPa]	C_{44} [GPa]
#1	3.559	3.315	1.243	1.334	0.900
#2	3.407	3.778	1.104	1.437	0.983

Table 7
Elastic constants of samples printed in variants #1 and #2 (transversely isotropic material model).

Variant	E_1 [GPa]	E_3 [GPa]	G_{31} [GPa]	G_{12} [GPa]	ν_{31} [–]	ν_{13} [–]	ν_{12} [–]
#1	2.857	2.574	0.900	1.158	0.278	0.308	0.234
#2	2.752	2.862	0.983	1.152	0.319	0.306	0.195

was performed repeatedly to cover the frequency range up to 400 kHz. To verify the results of optimisation, the theoretical (separated) curves for an optimal C_{13} value were superimposed on the experimental curves, altogether with the control points used for optimisation. The results are presented in Fig. 6. A good agreement between the experimental and theoretical approach is visible for both plates #P1 and #P2, which is an indication of the correctness of the calculations performed. Specific curves corresponding to certain symmetric (S_0, S_1,S_2) and antisymmetric (A_0, A_1) wave modes have been identified.

4.2.3. Calculation of elastic constants

The complete sets of elements of stiffness matrix **C** for variants #1 and #2 are presented in Table 6. Based on the determined elements, elastic constants were calculated using formulae (6)-(9). The results are given in Table 7. The first five constants are independent of each other and the remaining two constants depend on the first five. Since the raster angles of two consecutive layers were perpendicular in both printing variants, the elastic parameters were comparable. What is worth noting, the Young's modulus in the plane of symmetry was similar, however, the modulus along the symmetry axis was lower for #1 and higher for #2. This could be the effect of the local disturbance of wave propagation at the edges of the cubic samples. The results could be verified by the existing literature. Since no specific studies considering the samples produced with the same printing parameters were found, the elastic constants can be compared only roughly. In [14] some other works were referred, showing the range of elastic modulus mostly between 2.2 and 3.5 GPa, which agrees with our results. Some sources shown values of elastic modulus significantly lower (0.3 GPa) and significantly higher (9.5 GPa), however, these discrepancies resulted from the different sample sizes and test standards. Moreover, the producer's datasheet states that elastic modulus of used PLA filament varies between 3.0 and 3.4 GPa for different printing orientations (according to ASTM D3039 standard). Considering the geometry of samples and accuracy of production process, the reduction of the elastic modulus obtained in our research is acceptable.

4.3. Orthotropic material model (variant #3)

4.3.1. Identification of mechanical parameters based on bulk wave velocities

The samples produced in variant #3 did not meet the requirements of transverse isotropy, thus the orthotropic material model was used to characterise their mechanical behaviour. All of the P-wave velocities along the three axes *x*,*y*, *z* were different (see Table 4). The S-wave velocities in certain planes should be equal in pairs, however, but as the velocities along the *x* axis were indeterminable, this assumption was only verified for the *y*-*z* plane. The difference between $c_{T,y(z)}$ and $c_{T,z(y)}$ in relation to their mean value was equal to 1.00 %, so they were averaged and denoted as $c_{T,23}$. The two remaining velocities ($c_{T,y(x)}$ and $c_{T,z(x)}$) were taken directly and denoted as $c_{T,12}$ and $c_{T,13}$, respectively. As a result, six independent wave velocities were obtained for the sample printed with variant #3 (Table 8).

Table 8
P-wave and S-wave velocities for variant #3 (orthotropic material model).

Variant	$c_{L,1}$ [m/s]	$c_{L,2}$ [m/s]	$c_{L,3}$ [m/s]	$c_{T,12}$ [m/s]	$c_{T,13}$ [m/s]	$c_{T,23}$ [m/s]
#3	1368.1	1815.4	1733.6	880.0	720.9	1042.4

Because of the fact that there are six different velocities, six of the nine independent coefficients of the stiffness matrix could be determined (the diagonal ones). Using the formulae presented in Table 1 the diagonal elements are: C_{11} = 2.055 GPa, C_{22} = 3.619 GPa, C_{33} = 3.300 GPa, C_{44} = 1.193 GPa, C_{55} = 0.571 GPa, and C_{66} = 0.850 GPa. The non-zero elements off the main diagonal (C_{12}, C_{13}, C_{23}), which do not appear in Table 1 remained unknown.

4.3.2. Identification of remaining mechanical parameters based on dispersion curves

The missing elements of the stiffness matrix were determined based on the guided wave dispersion curves measured for plate #P3, as in variants #1 and #2. Since the mechanical parameters along the *x* axis (perpendicularly to the direction of filaments deposition) and *y* axis (along the direction of filament deposition) were different, dispersion curves had to be determined along both these directions (using traces A and B, as shown in Fig. 5). Experimental dispersion curves measured along the *y* axis and *x* axis are presented in Fig. 8a and Fig. 8b, respectively. The curves along the *y* axis have a good quality, similar to the curves in variants #1 and #2. However, the curves along the *x* axis have a significantly lower quality, because of the fact that the wave propagation was disturbed by the structure of the filament deposition (it propagated perpendicularly to the filament deposition direction). For this reason, control points were determined for the following characteristic frequencies equal to: 50 kHz, 150 kHz, 250 kHz, and 350 kHz for curves along the *y* axis and only for 50 kHz and 150 kHz for the *x* axis (see Fig. 8).

The theoretical dispersion curves were determined, as previously, using the SAFE method. The already defined diagonal elements of stiffness matrix **C** were used for the calculation. The elements off the main diagonal (C_{12}, C_{13}, C_{23}) were assumed to be in the range between 0 GPa and 2 GPa with a step of 0.01 GPa. Compared to the calculations for the transversely isotropic model, the step was increased to reduce the time of calculations, because a three-dimensional optimization would require a high computational cost. As before, the RSS function was calculated and minimized. Since RSS was a function of three variables, it was not possible to visualise it graphically in one diagram. For this reason, a few charts were prepared, representing the RSS function in relation to each individual variable, while the remaining two were heuristically set from the assumed range. It was observed that the RSS function obtained a clear minimum for C_{13} = 1.30 GPa and C_{23} = 1.01 GPa, while C_{12} seemed to not influence the RSS. In order to illustrate these relations, three example plots have been made showing the relations between RSS and each of the three variables, while the remaining two were indicating minimum (C_{12} was assumed to be equal to C_{13} for the purposes of this representation). The results are presented in Fig. 9. The relations between RSS and C_{13} (Fig. 9b) and C_{23} (Fig. 9c) showed a substantial influence of both variables on the dispersion curves. However, some disturbances were observed, resulting from the previously mentioned fact that multiple curves associated with different wave modes appear in the SAFE results. The RSS function was expected to be smooth (as observed in previous studies [31,32]), so the local sharp minima should not be considered, and the appropriate values were expected to be represented by local minima, which are clearly visible for both plots at C_{13} = 1.30 GPa, C_{23} = 1.01 GPa (as previously mentioned). In the case of C_{12} (Fig. 9a), the RSS function did not change significantly

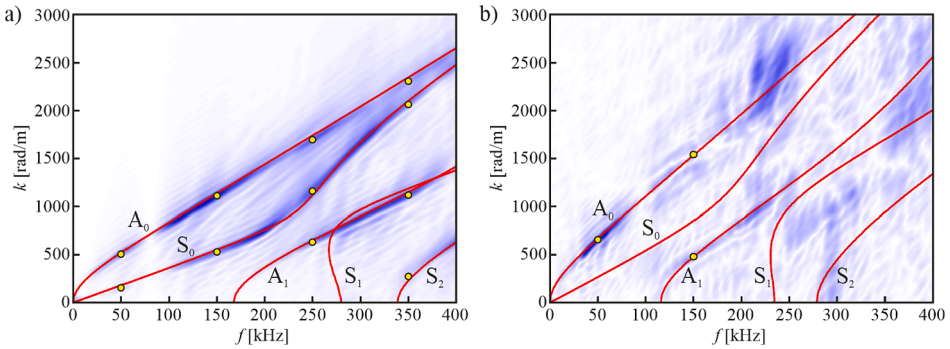

Fig. 8. Experimental dispersion curves (2D-FFT white-blue map) with control points (yellow circles) and theoretical dispersion curves from SAFE (red lines) for plate #P3: a) along the *y* axis (along the direction of filament deposition), b) along the *x* axis (perpendicularly to the direction of filament deposition).

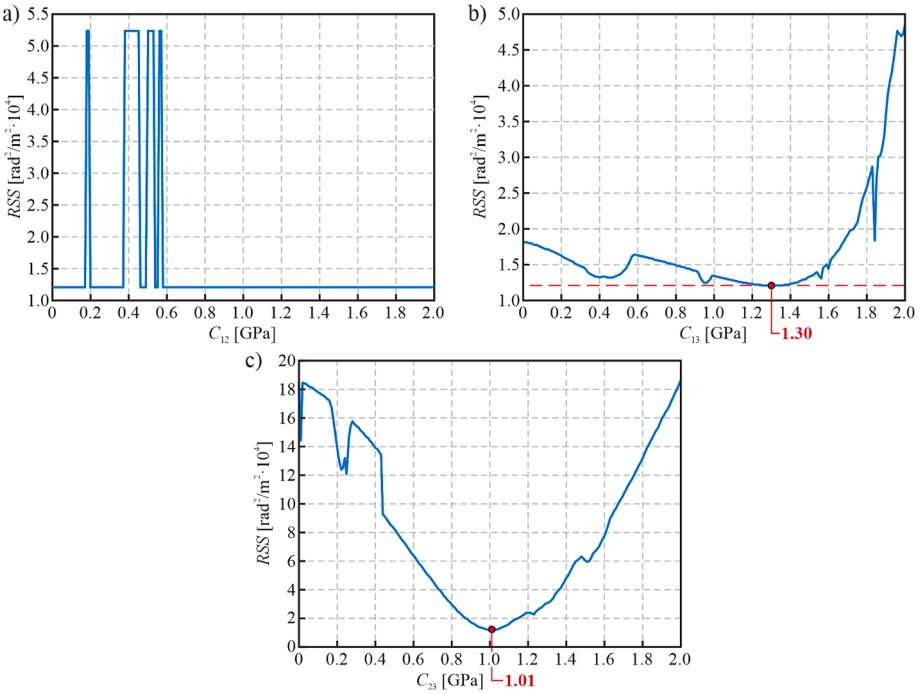

Fig. 9. Relation between RSS and optimized elements of stiffness matrix **C**: a) RSS vs. C_{12} (for $C_{13} = 1.30$ GPa, $C_{23} = 1.01$ GPa), b) RSS vs. C_{13} (for $C_{12} = 1.30$ GPa, $C_{23} = 1.01$ GPa), c) RSS vs. C_{23} (for $C_{12} = C_{13} = 1.30$ GPa).

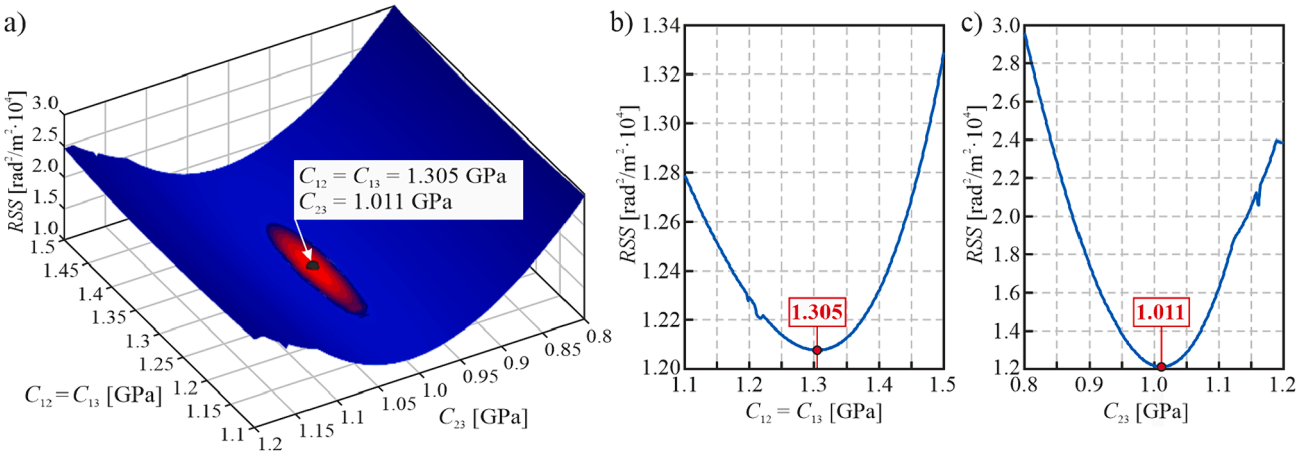

Fig. 10. Relation between RSS and optimized elements of stiffness matrix **C**: a) RSS vs. $C_{12} = C_{13}$ and C_{23}, b) RSS vs. $C_{12} = C_{13}$ (for $C_{23} = 1.011$ GPa), c) RSS vs. C_{23} (for $C_{12} = C_{13} = 1.305$ GPa).

Table 9
Elements of constitutive matrix **C** for variant #3 (orthotropic material model).

Variant	C_{11} [GPa]	C_{22} [GPa]	C_{33} [GPa]	C_{44} [GPa]	C_{55} [GPa]	C_{66} [GPa]	C_{12} [GPa]	C_{13} [GPa]	C_{23} [GPa]
#3	2.055	3.619	3.300	1.193	0.571	0.850	1.305	1.305	1.011

Table 10
Elastic constants of variant #3 (orthotropic material model).

Variant	E_1 [GPa]	E_2 [GPa]	E_3 [GPa]	G_{12} [GPa]	G_{31} [GPa]	G_{23} [GPa]	ν_{12} [–]	ν_{13} [–]	ν_{23} [–]	ν_{21} [–]	ν_{31} [–]	ν_{32} [–]
#3	1.291	2.777	2.459	0.850	0.571	1.193	0.274	0.312	0.074	0.588	0.594	0.065

and was constant with the exception of some sharp maxima. The function had no local minimum even when the scale was changed. This could be due to the fact that the curves corresponding to the wave modes dependent on C_{12} were not included in the analysis (only wave modes propagating in 1–3 and 2–3 planes were considered according to the calculations and experiments). In order to determine C_{12}, additional measurements are required for samples printed in different orientation to induce propagation of wave modes in 1–2 plane. However, it was not considered in the current study taking into account the difficulty of printing plate sample vertically.

To overcome the above-described issue, it was assumed that $C_{12} = C_{13}$, since the P-wave wave velocities along 2 and 3 axes were similar (see Table 8). This assumption reduced the dimension of the optimization problem from 3 to 2, allowing the calculations to be performed with a relatively low cost in terms of time. In this case, an additional optimization was performed with higher accuracy of 0.001 GPa in the range between 1.1 GPa and 1.5 GPa for $C_{12} = C_{13}$ and in the range between 0.8 GPa and 1.2 GPa for C_{23} (based on the evaluated initial values of the parameters). Fig. 10a shows the RSS as a function of two variables. A clear minimum was visible, indicating the optimum values of the calculation parameters: $C_{12} = C_{13} = 1.305$ GPa and $C_{23} = 1.011$ GPa. Additionally, two sections of the chart are shown in Fig. 10b,c, representing the RRS in relation to each variable, the second of which was optimal. The minima are present in both plots. As in the previous calculations, some disturbances can be identified, but their influence on the RSS function was irrelevant. The influence of C_{23} on the results was more pronounced, the RSS changes more significantly due to this value when compared to $C_{12} = C_{13}$.

Once the parameters C_{12}, C_{13} and C_{23}, had been determined, the calculation of the optimum dispersion curves was conducted using SAFE. As for variants #1 and #2, curve separation was performed and the curves corresponding to symmetric and antisymmetric wave modes were extracted. The final curves were compared with experimental results and control points (Fig. 8). A good agreement was observed for the dispersion curves in both directions. As for the previous variants, specific curves corresponding to certain wave modes were identified.

4.3.3. Calculation of elastic constants

After all calculations, the complete stiffness matrix was determined. All non-zero independent coefficients are listed in Table 9. The stiffness matrix was then inverted to obtain compliance matrix **S**. Based on its elements, the elastic constants were calculated according to Eq. (4). The elastic constants are given in Table 10. The first nine constants can be considered independent whereas the remaining three can be calculated based on the symmetry of the compliance matrix. The values can be compared with the results obtained for PLA by different authors. In [10] the elastic constants were (using the corresponding symbols): $E_1 = 1.542$ GPa, $E_2 = E_3 = 2.820$ GPa, $G_{12} = G_{13} = 0.715$ GPa, $\nu_{12} = 0.275$, $\nu_{13} = 0.293$, $\nu_{23} = 0.016$. Similar results were obtained in [13], where the elastic constants were equal to $E_1 = 1.460$ GPa, $E_2 = E_3 = 2.890$ GPa, $G_{12} = G_{13} = 0.817$ GPa, $\nu_{12} = 0.35$. There were some differences between the current results and those reported in previous works, but these could be the effect of the slightly different printing parameters, the 3D printer used and the filament producer. Taking these factors into account, the comparison was satisfactory.

5. Conclusions

The paper dealt with the problem of non-destructive identification of elastic parameters of additively manufactured samples. A two-stage ultrasound-based procedure was introduced. The elastic constants were determined by the combined experimental-theoretical approach, utilizing bulk wave velocities and guided wave dispersion curves. The study resulted in the conclusions presented below.

- The proposed method allowed the non-destructive characterisation of the mechanical behaviour of 3D printed samples satisfying the conditions of transversely isotropic and orthotropic material models. The analysis was conducted for three different variants of raster angles. The results were compared with the existing literature and showed satisfactory agreement.
- It was found that the proposed approach was robust and effective for elements meeting the conditions of the transversely isotropic material model. Due to the relative simplicity of the model, most of the elements of the stiffness matrix were determined by simple bulk wave velocity measurements on cubic samples, leaving one unknown coefficient, which was determined by optimising dispersion curves. The values Young's moduli varied between 2.6 and 2.9 GPa, shear moduli equalled between 0.9 and 1.2 GPa, whereas Poisson's ratios ranged between 0.20 and 0.32.
- The problem proved to be more complicated for the orthotropic model, as three elements remained unknown after the wave velocity measurements, making the optimization problem three-dimensional. Moreover, the dispersion curves were insensitive to one of the coefficients, which led to an inevitable simplification, i.e., assumption that two of the three unknown elements are equal, which was proved meaningful for the considered sample. The results were as follows: Young's moduli ranged between 1.3 and 2.8 GPa, shear moduli equalled between 0.6 and 1.2 GPa, and Poisson's ratios changed from 0.07 to 0.59. For the possible use of the proposed procedure for characterization of generally orthotropic materials, some modifications are required which leaves the field for further development of the described algorithm.

The results obtained will be further used to prepare numerical models of AM samples and numerical simulations of wave propagation, focusing on non-destructive damage detection and imaging in this type of elements. The proposed technique can be used to determine the elastic parameters of different materials, such as PEEK or PEKK, which will be verified in the future.

CRediT authorship contribution statement

Erwin Wojtczak: Writing – original draft, Visualization, Software, Methodology, Investigation, Funding acquisition, Formal analysis, Conceptualization. **Magdalena Rucka:** Writing – review & editing,

Supervision, Methodology, Investigation, Formal analysis, Conceptualization. **Angela Andrzejewska:** Resources, Methodology, Conceptualization.

Declaration of competing interest

The authors declare the following financial interests/personal relationships which may be considered as potential competing interests: Erwin Wojtczak reports financial support was provided by National Science Centre Poland.

Data availability

The raw data required to reproduce these findings are available to download from https://doi.org/10.34808/2g2j-8902. The processed data required to reproduce these findings cannot be shared at this time due to technical or time limitations.

Acknowledgements

This research was funded by National Science Centre, Poland, 2021/41/N/ST8/01348.

References

[1] Y.G. Jeong, W.S. Lee, K.B. Lee, Accuracy evaluation of dental models manufactured by CAD/CAM milling method and 3D printing method, J. Adv. Prosthodont. 10 (2018) 245–251, https://doi.org/10.4047/jap.2018.10.3.245.
[2] H. Yousef, B.T. Harris, E.N. Elathamna, D. Morton, W.S. Lin, Effect of additive manufacturing process and storage condition on the dimensional accuracy and stability of 3D-printed dental casts, J. Prosthet. Dent. (2021) 1–6, https://doi.org/10.1016/j.prosdent.2021.02.028.
[3] A. Haleem, M. Javaid, R.H. Khan, R. Suman, 3D printing applications in bone tissue engineering, J. Clin. Orthop. Trauma 11 (2020) S118–S124, https://doi.org/10.1016/j.jcot.2019.12.002.
[4] M. Meng, J. Wang, T. Sun, W. Zhang, J. Zhang, L. Shu, et al., Clinical applications and prospects of 3D printing guide templates in orthopaedics, J. Orthop. Transl. 34 (2022) 22–41, https://doi.org/10.1016/j.jot.2022.03.001.
[5] B. Deda Altan, G. Altan, V. Kovan, Investigation of 3D printed Savonius rotor performance, Renew. Energy 99 (2016) 584–591, https://doi.org/10.1016/j.renene.2016.07.043.
[6] V.S.R.P. Akula, K.K. Goyal, O.P. Verma, V. Gupta, Feasibility study of a 3D printed BLDC outrunner rotor, Mater. Today:. Proc. 80 (2023) 163–167, https://doi.org/10.1016/j.matpr.2022.11.090.
[7] G. Stano, G. Percoco, Additive manufacturing aimed to soft robots fabrication: a review, Extrem Mech. Lett. 42 (2021) 101079, https://doi.org/10.1016/j.eml.2020.101079.
[8] V.S. Joseph, T. Calais, T. Stalin, S. Jain, N.K. Thanigaivel, N.D. Sanandiya, et al., Silicone/epoxy hybrid resins with tunable mechanical and interfacial properties for additive manufacture of soft robots, Appl. Mater. Today 22 (2021) 100979, https://doi.org/10.1016/j.apmt.2021.100979.
[9] P. Biswas, S. Guessasma, J. Li, Numerical prediction of orthotropic elastic properties of 3D-printed materials using micro-CT and representative volume element, Acta Mech. 231 (2020) 503–516, https://doi.org/10.1007/s00707-019-02544-2.
[10] H. Gonabadi, Y. Chen, A. Yadav, S. Bull, Investigation of the effect of raster angle, build orientation, and infill density on the elastic response of 3D printed parts using finite element microstructural modeling and homogenization techniques, Int. J. Adv. Manuf. Technol. 118 (2022) 1485–1510, https://doi.org/10.1007/s00170-021-07940-4.
[11] M. Lei, Y. Wang, Q. Wei, M. Li, J. Zhang, Y. Wang, Micromechanical modeling and numerical homogenization calculation of effective stiffness of 3D printing PLA / CF composites, J. Manuf. Process. 102 (2023) 37–49, https://doi.org/10.1016/j.jmapro.2023.07.027.
[12] R. Torre, S. Brischetto, Experimental characterization and finite element validation of orthotropic 3D-printed polymeric parts, Int. J. Mech. Sci. 219 (2022) 107095, https://doi.org/10.1016/j.ijmecsci.2022.107095.
[13] A. Sabik, M. Rucka, A. Andrzejewska, E. Wojtczak, Tensile failure study of 3D printed PLA using DIC technique and FEM analysis, Mech. Mater. 175 (2022) 104506, https://doi.org/10.1016/j.mechmat.2022.104506.
[14] M. Piovan, F. Diaco, C. Nacud, L. Di Giorgio, Elastic properties of 3D printed pieces determined with dynamic methods: applications to assembled 3D printed structures, Int. J. Adv. Manuf. Technol. 109 (2020) 411–419, https://doi.org/10.1007/s00170-020-05649-4.
[15] F. Medel, V. Esteban, J. Abad, On the use of laser-scanning vibrometry for mechanical performance evaluation of 3D printed specimens, Mater. Des. 205 (2021) 109719, https://doi.org/10.1016/j.matdes.2021.109719.
[16] G. Krivic, J. Slavič, Simultaneous non-contact identification of the elastic modulus, damping and coefficient of thermal expansion in 3D-printed structures, Polym. Test. 125 (2023) 108131, https://doi.org/10.1016/j.polymertesting.2023.108131.
[17] Y.H. Huang, C.Y. Lin, Measurement of orthotropic material constants and discussion on 3D printing parameters in additive manufacturing, Appl. Sci. 12 (2022), https://doi.org/10.3390/app12136812.
[18] L. Qixian, J.H. Bungey, Using compression wave ultrasonic transducers to measure the velocity of surface waves and hence determine dynamic modulus of elasticity for concrete, Constr. Build. Mater. 10 (1996) 237–242, https://doi.org/10.1016/0950-0618(96)00003-7.
[19] P.P. Chavhan, M.R. Vyawahare, Correlation of compressive strength and dynamic modulus of elasticity for high strength SCC mixes, Int J Eng Tech Res 3 (2015) 42–46.
[20] J. Carrillo, J. Ramirez, J. Lizarazo-Marriaga, Modulus of elasticity and Poisson's ratio of fiber-reinforced concrete in Colombia from ultrasonic pulse velocities, J Build Eng 23 (2019) 18–26, https://doi.org/10.1016/j.jobe.2019.01.016.
[21] A.M. Lindrose, Ultrasonic wave and moduli changes in a curing epoxy resin, Exp. Mech. 18 (1978) 227–232, https://doi.org/10.1007/bf02328418.
[22] S. Dixon, D. Jaques, S.B. Palmer, The development of shear and compression elastic moduli in curing epoxy adhesives measured using non-contact ultrasonic transducers, J. Phys. D Appl. Phys. 36 (2003) 753–759, https://doi.org/10.1088/0022-3727/36/6/319.
[23] S. Dixon, D. Jaques, S.B. Palmer, G. Rowlands, The measurement of shear and compression waves in curing epoxy adhesives using ultrasonic reflection and transmission techniques simultaneously, Meas. Sci. Technol. 15 (2004) 939–947, https://doi.org/10.1088/0957-0233/15/5/023.
[24] T. Vogt, M. Lowe, P. Cawley, Cure monitoring using ultrasonic guided waves in wires, J. Acoust. Soc. Am. 114 (2003) 1303–1313, https://doi.org/10.1121/1.1589751.
[25] B. Mascaro, M.K. Budzik, M. Castaings, J. Jumel, M.E.R. Shanahan, Evaluation of adhesive bond Young's modulus during crosslinking using a mechanical method and an ultrasound method, J. Phys. Conf. Ser. 353 (2012), https://doi.org/10.1088/1742-6596/353/1/012006.
[26] Z.S. Tang, Y.Y. Lim, S.T. Smith, I. Izadgoshasb, Development of analytical and numerical models for predicting the mechanical properties of structural adhesives under curing using the PZT-based wave propagation technique, Mech. Syst. Sig. Process. 128 (2019) 172–190, https://doi.org/10.1016/j.ymssp.2019.03.030.
[27] K. Nakahata, Y. Amano, K. Ogi, K. Mizukami, T. Saitoh, Three-dimensional ultrasonic wave simulation in laminated CFRP using elastic parameters determined from wavefield data, Compos. B Eng. 176 (2019) 107018, https://doi.org/10.1016/j.compositesb.2019.107018.
[28] S. Wang, Z.t. Luo, J. Jing, Z.H. Su, X.K. Wu, Z.H. Ni, et al., Real-time determination of elastic constants of composites via ultrasonic guided waves and deep learning, Meas J Int Meas Confed 200 (2022) 111680, https://doi.org/10.1016/j.measurement.2022.111680.
[29] C. Huang, F. Lanza, An ultrasonic scanning system for the inspection of composite stiffened panels from elastic constant identification via inversion of guided waves, Compos. Struct. 322 (2023) 117373, https://doi.org/10.1016/j.compstruct.2023.117373.
[30] C. Gauthier, D. Leduc, J. Galy, M.E. Elkettani, J.L. Izbicki, Discrimination of epoxy curing by high lamb modes order, Phys. Procedia 70 (2015) 300–304, https://doi.org/10.1016/j.phpro.2015.08.159.
[31] E. Wojtczak, M. Rucka, Monitoring the curing process of epoxy adhesive using ultrasound and Lamb wave dispersion curves, Mech. Syst. Sig. Process. 151 (2021) 107397, https://doi.org/10.1016/j.ymssp.2020.107397.
[32] E. Wojtczak, M. Rucka, Damage imaging algorithm for non-destructive inspection of CFRP/steel adhesive joints based on ultrasonic guided wave propagation, Compos. Struct. 297 (2022) 115930, https://doi.org/10.1016/j.compstruct.2022.115930.
[33] W.H. Ong, N. Rajic, W.K. Chiu, C. Rosalie, Determination of the elastic properties of woven composite panels for Lamb wave studies, Compos. Struct. 141 (2016) 24–31, https://doi.org/10.1016/j.compstruct.2015.12.017.
[34] A. Gallina, L. Ambrozinski, P. Packo, L. Pieczonka, T. Uhl, W.J. Staszewski, Bayesian parameter identification of orthotropic composite materials using Lamb waves dispersion curves measurement, J. Vib. Control 23 (2017) 2656–2671, https://doi.org/10.1177/1077546315619264.
[35] Q. Chen, K. Xu, D. Ta, High-resolution Lamb waves dispersion curves estimation and elastic property inversion, Ultrasonics 115 (2021) 106427, https://doi.org/10.1016/j.ultras.2021.106427.
[36] A.H. Orta, J. De Boer, M. Kersemans, C. Vens, K. Van Den Abeele, Machine learning-based orthotropic stiffness identification using guided wavefield data, Meas J Int Meas Confed 214 (2023) 112854, https://doi.org/10.1016/j.measurement.2023.112854.
[37] P. Kudela, M. Radzienski, P. Fiborek, T. Wandowski, Elastic constants identification of woven fabric reinforced composites by using guided wave dispersion curves and genetic algorithm, Compos. Struct. 249 (2020) 112569, https://doi.org/10.1016/j.compstruct.2020.112569.
[38] P. Kudela, M. Radzienski, P. Fiborek, T. Wandowski, Elastic constants identification of fibre-reinforced composites by using guided wave dispersion curves and genetic algorithm for improved simulations, Compos. Struct. 272 (2021) 114178, https://doi.org/10.1016/j.compstruct.2021.114178.
[39] D.R. Foster, M.J. Dapino, S.S. Babu, Elastic constants of ultrasonic additive manufactured Al 3003–H18, Ultrasonics 53 (2013) 211–218, https://doi.org/10.1016/j.ultras.2012.06.002.
[40] H.R. Javidrad, S. Salemi, Determination of elastic constants of additive manufactured Inconel 625 specimens using an ultrasonic technique, Int. J. Adv.

Manuf. Technol. 107 (2020) 4597–4607, https://doi.org/10.1007/s00170-020-05321-x.
[41] D.N. Alleyne, P. Cawley, A 2-dimensional Fourier transform method for the quantitative measurement of Lamb modes, Proc IEEE Ultrason Symp 2 (1990) 1143–1146, https://doi.org/10.1109/ULTSYM.1990.171541.
[42] H. Song, J.S. Popovics, Characterization of steel-concrete interface bonding conditions using attenuation characteristics of guided waves, Cem. Concr. Compos. 83 (2017) 111–124, https://doi.org/10.1016/j.cemconcomp.2017.07.001.
[43] M.S. Harb, F.G. Yuan, A rapid, fully non-contact, hybrid system for generating Lamb wave dispersion curves, Ultrasonics 61 (2015) 62–70, https://doi.org/10.1016/j.ultras.2015.03.006.
[44] C. Gauthier, J. Galy, M. Ech-Cherif El-Kettani, D. Leduc, J.L. Izbicki, Evaluation of epoxy crosslinking using ultrasonic Lamb waves, Int. J. Adhes. Adhes. 80 (2018) 1–6, https://doi.org/10.1016/j.ijadhadh.2017.09.008.
[45] W.H. Ong, N. Rajic, W.K. Chiu, C. Rosalie, Lamb wave–based detection of a controlled disbond in a lap joint, Struct Heal Monit 17 (2018) 668–683, https://doi.org/10.1177/1475921717715302.
[46] J.L. Rose, Ultrasonic Guided Waves in Solid Media, Cambridge University Press, New York, 2014. https://doi.org/10.1017/CBO9781107273610.
[47] P. Bocchini, M. Asce, A. Marzani, E. Viola, Graphical user interface for guided acoustic waves, J. Comput. Civ. Eng. 25 (2011) 202–210, https://doi.org/10.1061/(ASCE)CP.1943-5487.0000081.
[48] S. Khan, I.M. Khan, I. Siddiqui, Speed of longitudinal and transverse plane elastic waves in rotating and non-rotating anisotropic mediums, World Appl. Sci. J. 15 (2011) 1761–1769.
[49] P. Chadwick, A prsl., Wave propagation in transversely isotropic elastic media - I. Homogeneous plane waves, Proc. R. Soc. London A Math. Phys. Sci. 422 (1989) 23–66, https://doi.org/10.1098/rspa.1989.0019.
[50] E. Wojtczak, M Rucka, A Andrzejewska, Measurements of ultrasonic bulk and guided wave propagation in additively manufactured cubes and plates obtained by ultrasonic pulse velocity analyzer and scanning laser vibrometry, Gdańsk University of Technology (2024), https://doi.org/10.34808/2g2j-8902.